

Characterization of an ultra cold neutron detector using scintillating lithium glass

Blair Jamieson^{a,*}, Lori Rebenitsch^a, Sean Hansen-Romu^a, Bernhard Lauss^b,
Thomas Lindner^{c,a}, Jeff Martin^a, Russ Mammei^a, Edgard Pierre^{d,c}

^a*University of Winnipeg*

^b*Paul Scherrer Institut*

^c*TRIUMF*

^d*Research Centre for Nuclear Physics, Osaka University*

Abstract

The efficiency of an ultra cold neutron detector using scintillating lithium glass was measured relative to a Cascade detector. The lithium glass detector was found to be $8.28 \pm 0.02(\text{stat}) \pm 2.00(\text{syst})\%$ more efficient than the Cascade detector for the ultra cold neutron source at Paul Scherrer Institut. In addition, an estimate of the absolute efficiency of background rejection is made as a function of rate. For the variable ultra cold neutron rate (varying from < 1 kHz to approx. 100 kHz per channel) and background rate seen at the Paul Scherrer Institut, we estimate that the absolute detector efficiency is $89.7^{+1.3}_{-1.9}\%$ and the background contamination is $0.3 \pm 0.1\%$.

Keywords: ^6Li , Cascade, UCN detector, Ultracold neutrons

1. Introduction

Determining the neutron Electric Dipole Moment (nEDM) limits theories beyond the Standard Model [1]. Ultra Cold Neutrons (UCN) provide a good means to determine the nEDM. As a result, there are various nEDM experiments around the world utilizing UCN that are either running or being planned [2, 3, 4, 5, 6, 7, 8, 9, 10, 11]. Measurements of the nEDM are limited by both the

*Please address correspondence to Blair Jamieson

Email address: bl.jamieson@uwinnipeg.ca (Blair Jamieson)

7 number of UCN produced and the efficiency of the detection system.

8 The UCN source at the Research Centre for Nuclear Physics (RCNP) in
9 Osaka successfully demonstrated UCN production in super fluid helium and
10 extraction through cold windows in 2013. This source is in the process of being
11 moved from RCNP to TRIUMF, in Vancouver, over the coming year where a
12 new UCN facility is being prepared. A neutron Electric Dipole Moment (nEDM)
13 experiment is planned as the first experiment after the source is installed at
14 TRIUMF.

15 A UCN detector using ^6Li glass has been designed and built for the nEDM
16 experiment. This detector must fulfill several performance requirements, includ-
17 ing the ability to dependably count UCN at high rates (> 1 MHz). In order
18 to determine the detector's performance, the detector has been benchmarked
19 against a Cascade detector using the UCN source at the Paul Scherrer Institut
20 (PSI) in Switzerland.

21 This paper will briefly describe the two detectors being compared in Sec-
22 tion 2. A comparison of the relative detector efficiency is described in Section 3.
23 Another goal of the tests is to estimate the overall detection efficiency and back-
24 ground rejection capabilities of the ^6Li detector. As the detectors reach higher
25 detection rates, the effects of pile-up and electronics dead-time need to be es-
26 timated, as detailed in Section 4. In order to understand the efficiency and
27 background rejection due to Pulse Shape Discrimination (PSD) used for the ^6Li
28 detector, a simulation of the UCN detection and background detection with the
29 ^6Li detector was prepared, as described in Section 5. To get an estimate of the
30 absolute detector efficiency, described in Section 6, we have taken account of
31 the PSD cut efficiency, along with estimates of the geometrical acceptance, and
32 neutrons lost to the lithium depleted layer of glass on top of the detector.

2. Overview of Detector Technology

2.1. Cascade Detector

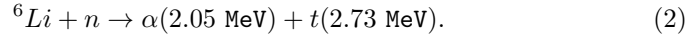
The Cascade detector, typically used at PSI to monitor UCN production, is a GEM-based neutron detector with multiple layers of ^{10}B coated GEM foils stacked, or “cascaded,” behind the each other. The boron captures the neutron and releases an α and ^7Li particles,



Due to the low Z materials, this detector picks up negligible γ background. The detector has with its own data acquisition system and had been tested previously with thermal neutrons [12].

2.2. ^6Li Scintillating Glass Detector

The scintillating glass uses ^6Li , which has a high neutron capture cross-section of order 10^5 bn [13, 14, 15], in the reaction:



In order to reduce the effect of an α or triton escaping the glass, two optically-bonded pieces of scintillating glass are used. The upper layer is depleted of ^6Li and the lower layer is doped with ^6Li to allow the resultant particles to deposit their full energy within the scintillating glass [15]. The scintillation light is then transferred via acrylic light-guide to its corresponding photomultiplier tube outside the detector vacuum region. The neutron capture scintillation gives a fast event signal with rise time of 6 ns and a fall time of about 40 ns [13]. There is, however, some late scintillation light up to 2 μs .

The detector design is similar to the detector at the PSI UCN source [13]. These detectors have some sensitivity to gamma-ray and thermal neutron backgrounds, as will be discussed in detail in this paper. Making the scintillating Li glass as thin as possible reduces its sensitivity to both thermal neutron captures and to γ -ray backgrounds. In addition, the gamma rays producing scintillation

58 light or Cerenkov light in the light-guides can be rejected by PSD since these
 59 signals are much shorter signals (FWHM approx. 20 ns) than the scintillation
 60 signal from the lithium glass.

61 In order to handle the high expected UCN rates, the ^6Li detector face is seg-
 62 mented into 9 channels. This reduces pile-up during high rates. A photograph
 63 and a drawing of the detector are show in Figure 1. The ^6Li glass side lengths
 64 of 29 mm can be used as a reference scale for the detector size.

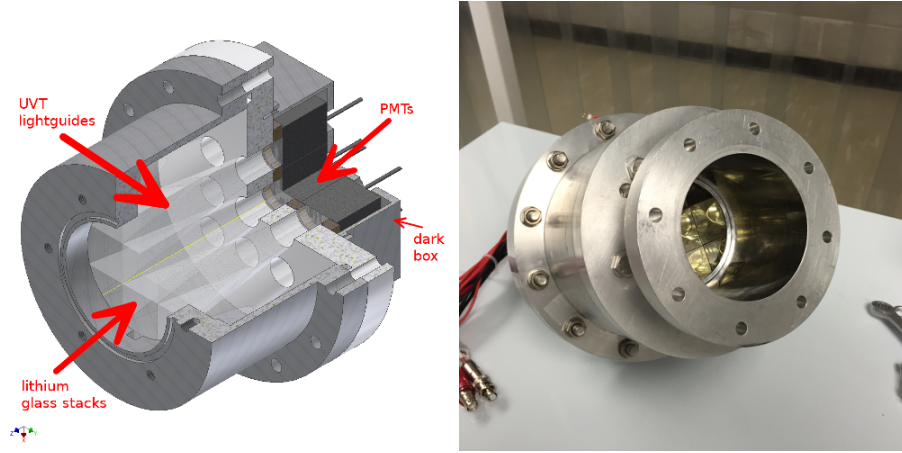


Figure 1: Three dimensional drawing of the UCN detector and enclosure (top), and a photo of the detector (bottom).

65 2.3. Overview of the Measurement Method

66 The PSI UCN source has two beam lines for testing, called “West-1” and
 67 “West-2.” West-2 offered UCN measurements of dropping UCN at varying
 68 heights, but at a lower rate. West-1 offered UCN at a much higher rate in a
 69 horizontal configuration, but only during times when the nEDM experiment at
 70 PSI was not using the UCN. The PSI UCN are produced by a 3 second long
 71 proton beam bunch every 300 seconds [16]. During the 297 seconds without the
 72 proton beam on target, the UCN diffuse down the beam line to the experiment
 73 area [17]. A typical UCN detector rate during a 300 second period in West-1 is
 74 shown in Fig. 2.

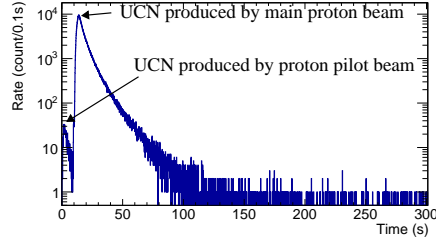


Figure 2: UCN produced during one proton beam irradiation of the spallation target, as detected with the Winnipeg ^6Li UCN detector on West-2.

Both the Cascade and ^6Li detectors were connect to each of these ports and collected data. PSI also had a Y-configuration available on West-2 which evenly split the beam between the detectors as shown in Figure 3. This allowed a more direct comparison of the data taking rates, and forms the basis of the comparison in this paper.



Figure 3: Configuration for splitting the UCN into two detectors. The Cascade detector is on the left and the ^6Li detector is on the right.

3. Relative rate comparison

Both detectors were placed in the y-configuration at the West-2 port to allow for a comparison of the averaged UCN rate over the course of the beam cycle for both detectors for the same cycle. The timing calibration between the two detectors' Data AcQuisition (DAQ) was done at the few second level by

85 comparing the time reported by the DAQ computers. A more close matching
86 of the time in the analysis of the data was performed at about the 0.05 s level
87 by aligning the times when the UCN rate was increasing after the main proton
88 beam irradiation of the spallation target.

89 The gross timing is confirmed by looking at the total count of UCN seen in
90 each detector per proton beam irradiation cycle. These counts are correlated as
91 are the times when a proton beam irradiation is skipped and both detectors do
92 not see UCN. Figure 4 shows the count of UCN detected in each 300 s cycle by
93 each of the detectors.

94 Note that ${}^6\text{Li}$ detector connects to the UCN source with a 75 mm diameter
95 guide, while the Cascade detector connects with a 70 mm guide. To account
96 for this difference, the count seen by the ${}^6\text{Li}$ detector is also shown scaled down
97 by the ratio of areas. This comparison shows that the relative count of UCN
98 from the PSI source was changing over the course of this data collection pe-
99 riod, and that for the spectrum of UCN in this beamline for the ${}^6\text{Li}$ detector is
100 $10.279 \pm 0.024(\text{stat})\%$. While the y-configuration is as direct a comparison as
101 could be obtained, however simulations indicate there is a $-2.0 \pm 2.0\%$ system-
102 atic difference due to the additional connectors required to reduce the 75 mm
103 diameter guide to 70 mm diameter for the Cascade detector. Overall the lithium
104 detector is $8.28 \pm 0.02(\text{stat}) \pm 2.00(\text{syst})\%$ more efficient for the UCN from the
105 PSI source.

106 In addition to the comparison of the count for a whole 300 second cycle,
107 the UCN detection rate in 0.1 second bins since the beginning of the beam
108 cycle averaged over 132 beam cycles is compared, as shown in Fig. 5. This
109 comparison includes the area normalization, and shows that the ${}^6\text{Li}$ detector
110 appears to detect more UCN at higher rates at earlier times since the UCN
111 production than the Cascade detector. We attribute the lower rate at later
112 times to the difference in the Fermi potential of the two detectors. The ${}^6\text{Li}$
113 detector's lithium depleted glass, which is the first material that the UCN see
114 has a Fermi potential of 107 neV, while the Cascade detector has an Al window
115 with an effective Fermi potential of 54 neV. The faster UCN reach the detectors

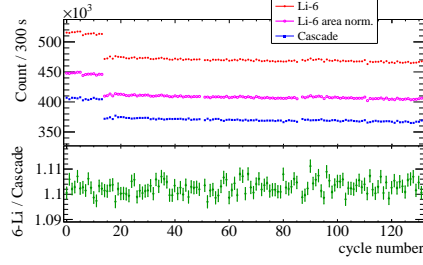


Figure 4: Detected UCN count per 300 second cycle is shown in the top panel for the ^6Li detector (red filled circles), Cascade detector (blue filled squares), and the area normalized ^6Li count (magenta open circles). The bottom panel shows the ratio of the area normalized count in the ^6Li detector to the Cascade detector (colour online).

116 sooner, and the ^6Li detector's performance for the higher energy UCN is better
 117 than the Cascade detector. However, later in the beam cycle, the UCN spectrum
 118 is softer, and the lower energy UCN are not seen by ^6Li detector, making the
 119 Cascade detector more efficient for lower energy UCN (below 107 neV).

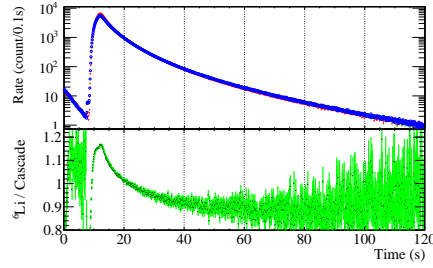


Figure 5: UCN Detection count per 0.1s averaged over 130 UCN cycles. The top panel shows an overlay of the area normalized ^6Li data in Red with the Cascade data in blue. The bottom plot shows a ratio of ^6Li count over Cascade count in each 0.1 s interval.

120 Another possible reason for the difference in detection efficiency as a function
 121 of rate is that the Cascade detector has a time event window of 400 ns while the
 122 ^6Li detector has a time event window of 200 ns. Changing the ^6Li detector's
 123 time event window to 400 ns or 800 ns did lengthen the event rate at the tail of
 124 the beam cycle.

125 4. Calculating the number of pile-up and dead-time events

126 Consider two independent rates of events, a rate of signal events and a rate
 127 of background events. Given a running time and detection window time, this
 128 section reviews the analytic calculation of the number of single signal, single
 129 background, the various combinations of multiple signal and background events,
 130 and the number of events during the dead-time.

131 4.1. Calculating the rates based on random Poisson processes

132 Consider a rate of signal events, R_{sig} . For a given running time, T , the
 133 number of expected signal events is $\nu_{\text{sig}} = R_{\text{sig}}T$. If a detector collects the
 134 signal over a gate with a width in time, t_{LG} , then in any of these gates the
 135 average number of events in that time interval is $n_{\text{sig}} = R_{\text{sig}}$. Each time the
 136 electronics triggers on a pulse from the detector it is dead for a time t_{dead} after
 137 the width of the collection gate.

As a final effect, for some fraction of the events detected, there is a second
 trigger (a re-trigger) on late light. The number of these events is some fixed
 fraction, f_{retrig} , of the single signal events. This fraction depends on the signal
 event threshold, but once determined for a given threshold, does not depend
 on the rate of events (only on the total number of events). The number of late
 light re-triggers is:

$$\nu_{\text{retrig}} = f_{\text{retrig}}\nu_{\text{sig}}. \quad (3)$$

138 The different combinations of events in a given running time, T , that are
 139 being considered are those that have:

- 140 1. a single signal event, ν_{1sig} ,
- 141 2. multiple signal events, $\nu_{N\text{sig}}$,
- 142 3. a single background events, ν_{1bg} ,
- 143 4. multiple background events, $\nu_{N\text{bg}}$,
- 144 5. a single signal plus a single background event, ν_{1sig1bg} , and
- 145 6. one or more signal events during the dead-time, ν_{dead} .

146 The rate of signal and background events each has an expected average number
 147 of events in any time interval that is a random process.

148 In any time interval, T , the number of single signal events measured, N_{sig} ,
 149 follows a Poisson distribution of the form:

$$P(N_{\text{sig}}, \nu_{\text{sig}}) = \exp(-\nu_{\text{sig}}) \frac{\nu_{\text{sig}}^{N_{\text{sig}}}}{N_{\text{sig}}!}.$$

The expected number of single signal events is defined to be:

$$\nu_{\text{sig}} = R_{\text{sig}}T. \quad (4)$$

150 Similarly, the number of single background events, N_{bg} , follows a Poisson
 151 distribution:

$$P(N_{\text{bg}}, \nu_{\text{bg}}) = \exp(-\nu_{\text{bg}}) \frac{\nu_{\text{bg}}^{N_{\text{bg}}}}{N_{\text{bg}}!}.$$

The expected number of single background events is defined to be:

$$\nu_{\text{bg}} = R_{\text{bg}}T. \quad (5)$$

152 For the multiple signal events in a single gate, consider the probability of
 153 having more than one signal event in the time interval of the gate. In any
 154 randomly placed gate, the expected average number of signal events is $\bar{n}_{\text{sig}} =$
 155 $t_{\text{LG}}R_{\text{sig}}$. The gates are not randomly distributed, instead they occur if there
 156 already was a signal event that triggered the gate. Therefore for each of the
 157 N_{sig} signal events there is a probability of having more than one additional
 158 signal event of:

$$P(n_{\text{sig}} > 0, \bar{n}_{\text{sig}}) = 1 - P(0, \bar{n}_{\text{sig}}) = 1 - \exp(-\bar{n}_{\text{sig}}).$$

159 This is one minus the probability of having zero extra signal pulses in the
 160 gate. The probability above is multiplied by the average number of single signal
 161 events, giving the expected average number of multiple signal triggers:

$$\nu_{\text{Nsig}} = \nu_{\text{sig}}(1 - \exp(-\bar{n}_{\text{sig}})).$$

162 Plug in the number of expected events in a randomly placed gate to get the
 163 final result:

$$\nu_{\text{Nsig}} = \nu_{\text{1sig}}(1 - \exp(-t_{\text{LG}}\nu_{\text{1sig}}/T)). \quad (6)$$

Using a similar argument for multiple background events, on average, the result is:

$$\begin{aligned} \nu_{\text{Nbg}} &= \nu_{\text{1bg}}(1 - \exp(-\bar{n}_{\text{bg}})) \\ &= \nu_{\text{1bg}}(1 - \exp(-t_{\text{LG}}\nu_{\text{1bg}}/T)). \end{aligned} \quad (7)$$

164 The number times we get a single neutron and a single gamma is calculated
 165 as a sum of two terms. The first term is the number of times we get a single
 166 signal event times the probability of getting a single background event in a
 167 randomly placed gate. The second term is the number of times we get a single
 168 background event times the probability of getting a single signal event in a
 169 randomly placed gate. On average the number of these events is:

$$\begin{aligned} \nu_{\text{1sig1bg}} &= \nu_{\text{1sig}} \exp(-t_{\text{LG}}\nu_{\text{1bg}}/T) t_{\text{LG}}\nu_{\text{1bg}}/T + \\ &\quad \nu_{\text{1bg}} \exp(-t_{\text{LG}}\nu_{\text{1sig}}/T) t_{\text{LG}}\nu_{\text{1sig}}/T. \end{aligned} \quad (8)$$

Finally, the number of dead-time signal events, ν_{dead} , can be calculated in a similar manner to the pile-up, ν_{Nsig} . Assume the total number of triggers is dominated by the single signal or single background events: $\nu_{\text{1sig}} + \nu_{\text{1bg}}$. For each of these triggers, the average number of signal events during a dead time is $\bar{n}_{\text{dead}} = t_{\text{dead}}R_{\text{sig}}$. Each of the triggers has a Poisson probability of having one or more signal events during the dead time:

$$\begin{aligned} P(n_{\text{dead}} > 0, \bar{n}_{\text{dead}}) &= 1 - P(0, \bar{n}_{\text{dead}}) \\ &= 1 - \exp(-\bar{n}_{\text{dead}}). \end{aligned}$$

Again, this is just one minus the probability of having zero extra signal pulses in the time period after any gate. Multiply the above probability times

the number of triggers, and we expect, on average, to have the number of dead-time neutrons:

$$\nu_{\text{dead}} = (\nu_{\text{sig}} + \nu_{\text{bg}}) \cdot (1 - \exp(-t_{\text{dead}}\nu_{\text{sig}}/T)). \quad (9)$$

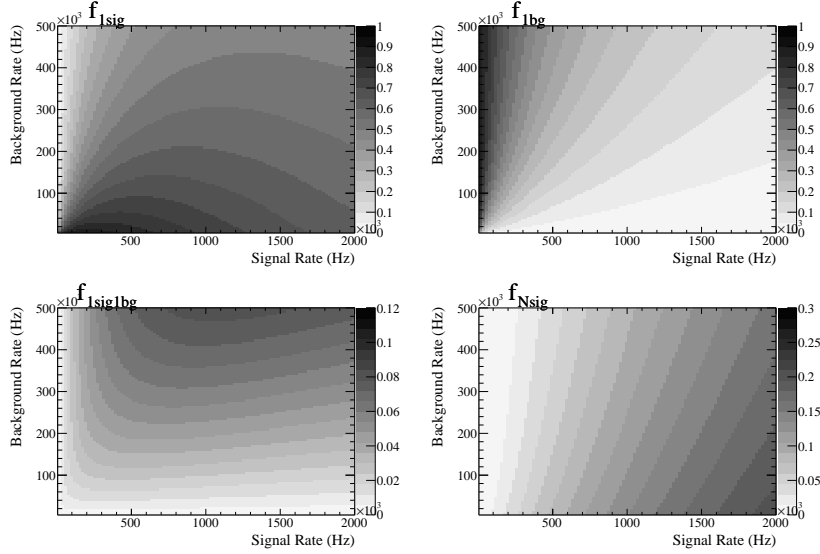


Figure 6: Fraction of events as a function of rate, going from top to bottom are for: single signal events, single background events, 1 signal and 1 background events, and multiple signal events.

4.2. Calculations to test the rate equations

In this section plots of the ratio of the number of events to the total number of events as a function of signal rate and background rate are plotted. These plots are made as a contour map, with y -axis being the signal rate, R_{sig} , the x -axis being the background rate, and the z -axis being the fraction of the triggers of the given type. These plots are made for each of the seven categories of events.

For these plots we will use the settings that were used for the digitizer in the measurements at PSI. The relevant settings are, $t_{\text{LG}} = 200$ ns, $t_{\text{dead}} = 150$ ns, and $f_{\text{retrig}} = 0.1$. For these gate times, consider what happens when there is

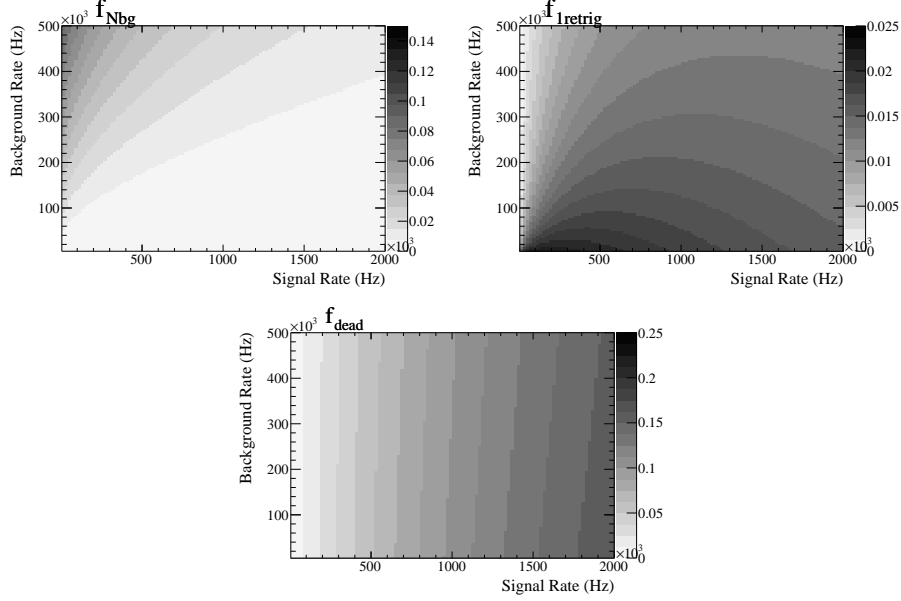


Figure 7: Fraction of events as a function of rate, going from top to bottom are for: N background events, re-trigger on late light (set at 2.5%), and dead time signal events.

a high signal rate of $R_{\text{sig}} = 1/t_{\text{LG}} = 5$ MHz with no background. After an arbitrary $T = 10$ s of running at this rate the number of single signal events is $\nu_{\text{1sig}} = R_{\text{sig}}T = 10^7$ events. On average the number of times there is a multiple signal events is given by Eq. 6:

$$\nu_{\text{Nsig}} = 10^7(1 - \exp(-2^{-7} \text{ s} \cdot 10^7/10 \text{ s})) = 1.8 \times 10^6. \quad (10)$$

177 This seems reasonable that there would be a large fraction of the events ($\sim 18\%$)
 178 that would have more than one neutron.

179 In calculating the fractions of events we use for the denominator, the total
 180 average (expected) number of triggers as a function of rate:

$$\nu = \nu_{\text{1sig}} + \nu_{\text{Nsig}} + \nu_{\text{1bg}} + \nu_{\text{Nbg}} + \nu_{\text{1sig1bg}} + \nu_{\text{dead}} + \nu_{\text{retrig}}. \quad (11)$$

181 In equation 11 each term can be calculated using Eqs. 3 to 9, which may
 182 depend on the signal and background rates. For example the fraction of single

183 signal events is then given by:

$$f_{\text{sig}} = \frac{\nu_{\text{sig}}}{\nu}. \quad (12)$$

184 Similar expressions can be written for the fractions of each of the event types.
 185 Fig. 6 and Fig. 7 show the fraction of each type of event as a function of signal
 186 and background rate.

187 5. Scintillation and light-guide background simulation

188 In order to build distribution functions for late light events, multiple signal
 189 events, and combinations of signal and background events, a detailed simulation
 190 of the pulses and the digitizer was developed. A single photo-electron was
 191 assumed to produce a Gaussian pulse with an amplitude drawn from a Gaussian
 192 with mean and width, $A = 20$ mV, and accepting only amplitudes above 4 mV.

A single scintillation signal event's pulse was then built assuming that the arrival times of each photo-electron from the scintillation signal followed some rise time, $\tau_R = 6.4$ ns, a fast scintillation fall time, $\tau_F = 41.752$ ns, and a slow scintillation fall time, $\tau_S = 2000$ ns. The probability, $P(t)$, of having a photo-electron at a given time, t , when the scintillation light starts arriving at time, T , was drawn from the distribution:

$$P(t) = \begin{cases} A(1 - e^{-(t-T)/\tau_R}), & T < t < T + 5\tau_R \\ A((1 - f_L)e^{-(t-T-5\tau_R)/\tau_F} + f_L e^{-(t-T-5\tau_R)/\tau_L}), & t \geq T + 5\tau_R. \end{cases} \quad (13)$$

193 The fraction of the scintillation light in the late light was $f_L = 1\%$. All of the
 194 values used in the simulation, as described above, were chosen to best match
 195 the data. The number of photo-electrons for a single neutron event was drawn
 196 from a Poisson distribution with mean number of photo-electrons of 83. The
 197 distribution of scintillation photo-electron arrival times along with a sample
 198 pulse is shown in the left panel of Fig. 8.

199 A single background event was modelled as having a Gaussian pulse with
 200 $\sigma = 6.4$ ns for the times of each photo-electron. Again, each photo-electron

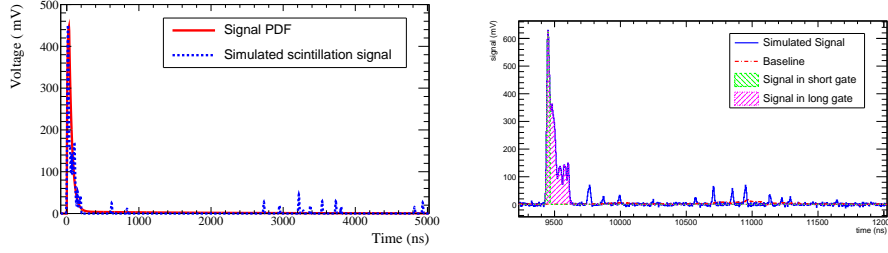


Figure 8: Simulated scintillation signal (blue dashed) and distribution function used to generate it (red solid) is shown in the left panel. The right panel shows the digitizer treatment of another simulated signal (solid line), where the baseline calculation (red dot-dashed line), signal within the short gate (green right-diagonal fill) and signal within the long gate (magenta left-diagonal fill) are shown.

was treated as a Gaussian with a random amplitude drawn from a Gaussian with mean and width of $A = 20$ mV, and accepting only amplitudes above 4 mV. The number of photo-electrons for the background signal was drawn from an exponential distribution with an average of 7.5 photo-electrons. This distribution was chosen to match the dominant component of the background observed in data.

The simulation of the pulses was used to generate 0.1 second long sets of data where the signal and background pulses were generated at a specified random rate. These simulated data were then sent to a digitizer simulation, described in the following section.

5.1. Digitizer simulation

The CAEN V1720 digitizer with the PSD firmware samples the waveforms every 4 ns, and for each sample digitizes the voltage on a ± 1 V scale into an ADC value between 0 and 4096. Each channel of the digitizer can trigger on its signal based on going some number of ADC counts below a pedestal value. In the simulation the threshold was set at 250 ADC (~ 125 mV). The digitizer can be run with a fixed pedestal, or simpler to set up, a pedestal taken from an average over the last 32 samples. This self calculated pedestal is called a baseline

219 in the digitizer documentation, and once a trigger happens, the baseline is held
 220 constant until the end of a specified gate time.

The PSD firmware calculates the sum of the signal below the threshold for a short gate width, $t_s = 40$ ns, and for a long gate width, $t_L = 200$ ns, after the trigger. The ADC sum below threshold within the short gate is called, Q_S , and the sum within the long gate is called, Q_L . The PSD value is also calculated, and defined as:

$$\text{PSD} = \frac{(Q_L - Q_S)}{Q_L}. \quad (14)$$

221 After each trigger, the digitizer channel is busy for a 150 ns dead-time. An
 222 example of the signal within each of the gates is depicted in the right panel of
 223 Fig. 8. A cut on the values of the charges Q_L and PSD provides a rejection of
 224 gamma interactions with the lighguides.

225 As outlined in the section describing the rates seven categories of events are
 226 considered. Simulated electronic pulses for each of these possible combinations
 227 is shown in Fig. 9 and Fig. 10.

228 5.2. Probability distribution functions from the simulations

229 The combination of the signal and background pulse simulations with the
 230 digitizer simulation is used to generate probability distribution functions in the
 231 PSD versus Q_L space for each of the different possible combinations of events.

232 To limit the number of possible PDFs, an approximation of the higher event
 233 multiplicities within a single gate is included in a single PDF. These multiple
 234 signal or multiple background PDFs could change shape if the rate of events is
 235 changed by over a few orders of magnitude, but is treated as fixed in estimating
 236 the detector performance.

237 Using a collection of randomly generated signal and background events, the
 238 PDFs for each of the signal types was generated. In the case of the single back-
 239 ground event, it was possible to use the data from beam cycles with proton-beam
 240 off, when there was no UCN produced. The rest of the PDFs were generated
 241 after tuning the simulation to match the data. In the simulation the average

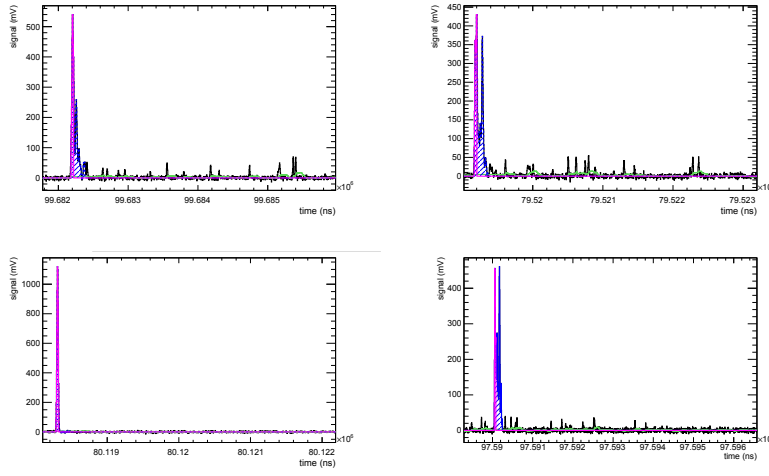


Figure 9: Simulated signals seen by the ${}^6\text{Li}$ detector in mV versus time for different combinations of signal and background events. The magenta left-diagonal-hatched region represents the Q_S portion of the signal, the blue right-diagonal-hatched region represents Q_L , and the green line (colour online) represents the average baseline. From top to bottom right the plots show: a single signal event, a multiple signal event, a single background event, and a multiple background event.

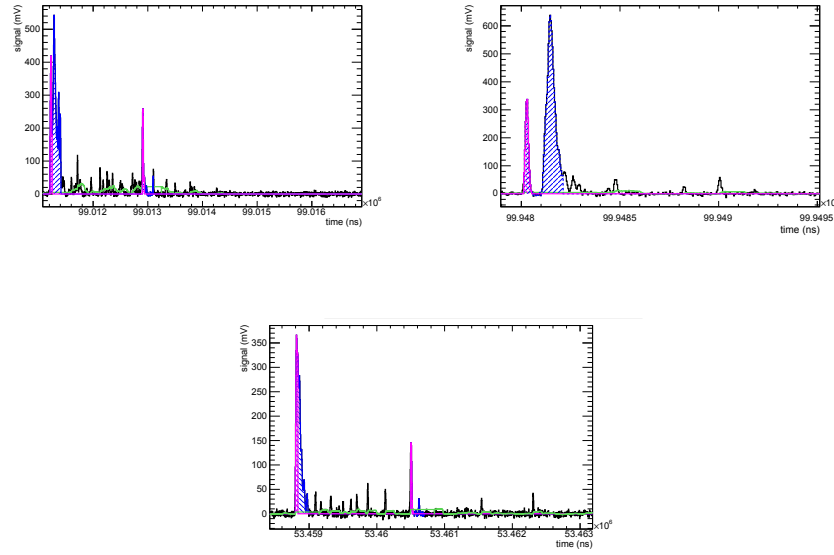


Figure 10: From top to bottom these plots show: a single signal plus single background event, a dead-time event, and a late-light re-trigger event.

number of photo-electrons per neutron capture, the fall time of the fast scintillation signal, the fall time of the long scintillation signal, the average number of photo-electrons in the background were all tuned. In addition, the average charge in the signal measured by the detector, from each channel, was scaled to match the mean value in the simulation (as a gain matching).

The PDFs for the different combinations of signal and background are compared to data as shown in Fig. 11. A template fit of these PDFs to estimate amount of signal and background in the data is possible.

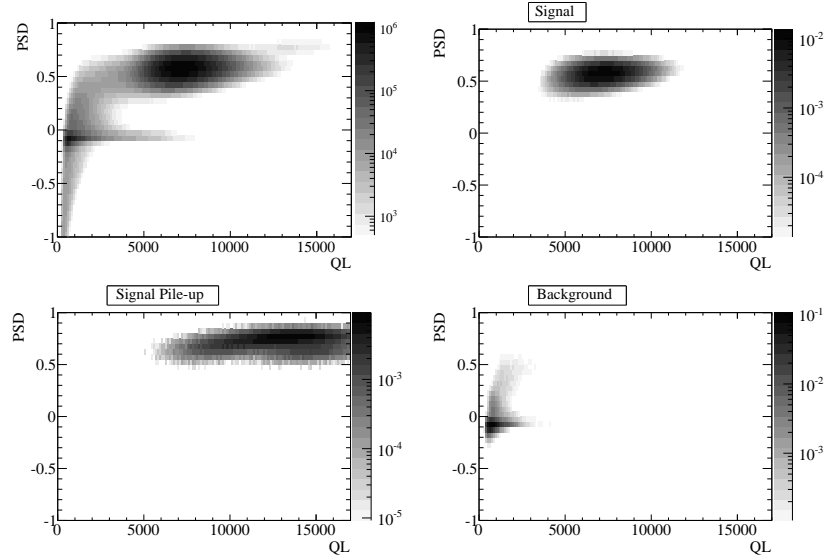


Figure 11: Event count (or relative event count) as a function of PSD and Q_L , going from top to bottom is for UCN data, single neutron simulation, N neutron simulation, and background (from data taken during cycles without proton beam).

6. Estimate of the absolute detector efficiency and background contamination

In order to determine the UCN detection efficiency of the ^6Li the active area of the detector, losses due to absorption in the front face, and neutrons lost due to the background rejection cuts need to be considered. In principle one also

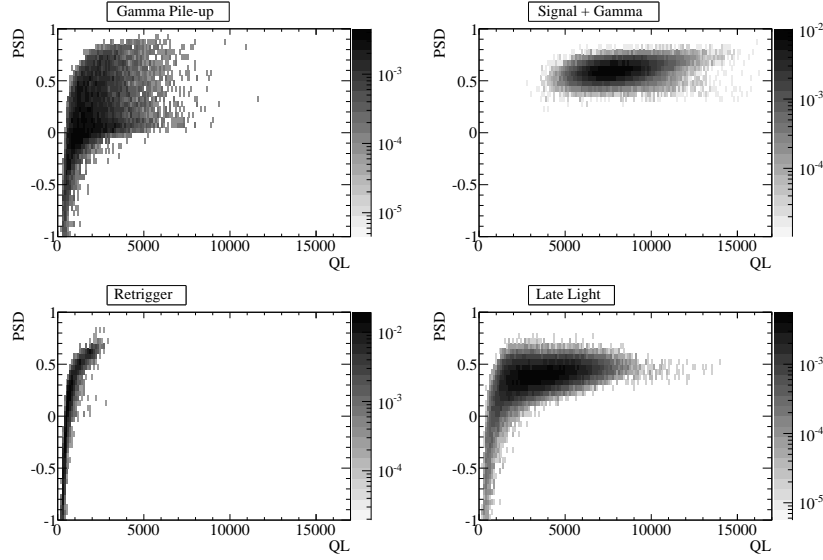


Figure 12: Event count (or relative event count) as a function of PSD and Q_L , going from top to bottom is for N background simulation, single neutron plus single background simulation, dead-time neutron simulation, and re-trigger on late light simulation.

has to take into account the spectrum of UCN that are being detected. Here we will assume that we want to know the efficiency for detecting UCN with kinetic energy above the effective Fermi potential of the lithium glass (~ 107 neV). Then if one has a known spectrum of UCN, the efficiency for detecting could be estimated as zero for the UCN below 107 neV, and the value we estimate here for those above 107 neV.

6.1. Detector effective area

The estimate of the detector's effective area comes from a photograph of the front face of the detector, where the side length of each of the squares of ^6Li glass is 29.0 ± 0.1 mm. Using this known length the pixels in the photograph that make up the circular aperture of the detector are counted as the denominator, and the count of pixels containing lithium glass as the numerator. A photograph of the detector face, that has been put in grey-scale, is shown in Fig. 13. From this image the estimated active area of the detector is $97.4 \pm 0.1\%$ of the whole

269 aperture.

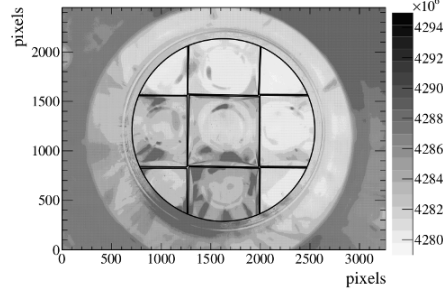


Figure 13: Gray-scale image of the detector face used for estimating the areal efficiency of the detector. The detector aperture and edges of the lithium glass are identified by the black lines.

270 6.2. Estimation of UCN absorption in Li depleted layer

271 The cross section for absorption of UCN on ${}^6\text{Li}$ is $\sigma = (4.5 \pm 2.5) \times 10^5$ barns[13].
 272 The company contracted to thin our samples of lithium glass has estimated our
 273 GS30 (lithium glass depleted in ${}^6\text{Li}$) layer to be $(55 \pm 10) \mu\text{m}$ thick. Given that
 274 the lithium content in GS30 is $N = 2.4 \times 10^{-24} \text{ cm}^{-3}$, the absorption length,
 275 $\lambda = 1/(N\sigma)$, is $\lambda = 1.35 \pm 0.75 \text{ cm}$. The fraction of UCN making it through our
 276 GS30 layer is calculated to be $99.34 \pm 0.43 \%$.

277 Measurements of the transmission of UCN through different thicknesses of
 278 GS30 have been conducted at the Institut Laue-Langevin in Grenoble[18]. Using
 279 their measurements, for a $55 \pm 10 \mu\text{m}$ GS30 layer the UCN transmission is
 280 $92.6^{+1.2}_{-1.8}\%$. The uncertainty is asymmetric due to the exponential nature of
 281 the attenuation through a layer with uncertain thickness. The measurements
 282 suggest that the UCN loss through a GS30 layer is not dominated by the ${}^6\text{Li}$
 283 content, but by losses by some other unidentified mechanism.

284 6.3. PSD cut efficiency and background rejection

285 The PSD and Q_L cut efficiency for keeping UCN, and background contami-
 286 nation remaining is estimated using an extended maximum likelihood fit of the
 287 PDF templates described in Section 5. The PDFs, binned in PSD and Q_L , are

288 labelled as $P_i(PSD, Q_L)$, where $i=(1 \text{ sig}, N \text{ sig}, 1 \text{ bg}, N \text{ bg}, 1 \text{ sig } 1 \text{ bg}, \text{dead},$
 289 or retrigger). The number of each type of event is estimated as N_i by minimizing
 290 a negative log likelihood that is calculated as a sum over all M of the PSD^j and
 291 Q_L^j measurements in the data as:

$$-\ln(L) = \sum_i^7 N_i - \sum_j^M \ln \sum_i^7 P_i(PSD^j, Q_L^j). \quad (15)$$

292 A projection of the results onto the PSD and Q_L axes for one of these fits
 293 is shown in Fig. 14. All of the features seen in the data are reproduced in the
 294 fit, although the reduced chi-squared of the fit is rather poor. We attribute the
 295 differences to details that are not properly modelled, such as any contribution
 296 from light leaks, PMT after-pulsing, and differences in gain variation between
 297 the nine channels of the detector.

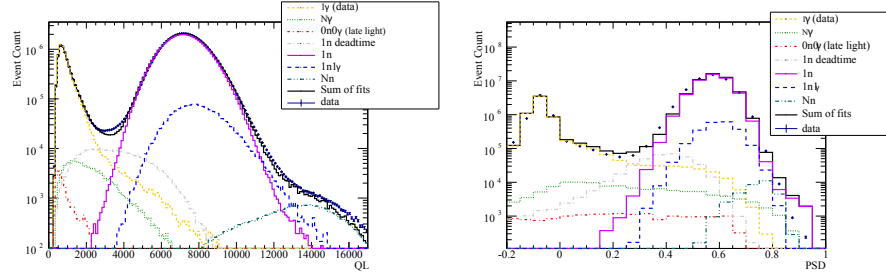


Figure 14: Template fit results in the one dimensional projections along the total event charge (top) and along the PSD (bottom).

298 *Cut detection efficiency and background rejection estimates.* Using the tem-
 299 plate fit, the neutron detection efficiency and background contamination are
 300 computed for different cut values in PSD and Q_L . The signal templates, in
 301 addition to single neutrons, are taken to include Nn, dead-time neutrons and
 302 1n1 γ events. The background rates are extracted from the 1 γ , late light, and
 303 N γ templates. If the total number of neutrons in the templates is N_n , and the
 304 number of neutrons above a given cut value is N_n^{cut} , then the neutron efficiency

305 due to background rejection cuts is defined as:

$$\epsilon_n = \frac{N_n^{cut}}{N_n}. \quad (16)$$

306 If the number of events in the background templates above a given cut value is
 307 N_γ^{cut} , then the background contamination fraction is defined as:

$$\eta_\gamma = \frac{N_\gamma^{cut}}{N_n}, \quad (17)$$

308 and the background rejection as:

$$\epsilon_\gamma = 1 - \eta_\gamma. \quad (18)$$

309 Figure 15 shows the neutron efficiency and background contamination of the
 310 entire beam pulse spectrum for two PSD cuts. For a cut $Q_L > 3000$ ADC
 311 and $PSD > 0.3$, the neutron acceptance is $99.5 \pm 0.5\%$ and the background
 312 contamination is $0.3 \pm 0.1\%$.

313 The rate of neutrons varies over the 300 second cycle of the UCN produced
 314 at PSI. To study the neutron detection efficiency and background contamination
 315 at different rates, the data was split into three time periods after the proton
 316 beam irradiation: high rate, middle rate, and low rate. The split data was fitted
 317 according to the template fit and then the efficiency was calculated according
 318 to each fit. The low rate data had more background contamination than the
 319 other rates, presumably due to the higher ratio of background to signal events.
 320 Using a cut on $Q_L > 3000$ ADC and $PSD > 0.3$, the neutron efficiency was
 321 $99.5 \pm 0.5\%$ and the background contamination was $0.3 \pm 0.1\%$.

322 The ${}^6\text{Li}$ detector therefore has a very good background rejection due to
 323 the signal shape variation between lightguide background and the scintillation
 324 events from the lithium glass.

325 6.4. Overall Detector Efficiency Estimate

326 The overall detection efficiency, for the rates of UCN at PSI, including all
 327 of the effects described in this section, is $89.7^{+1.3}_{-1.9}\%$, which is dominated by

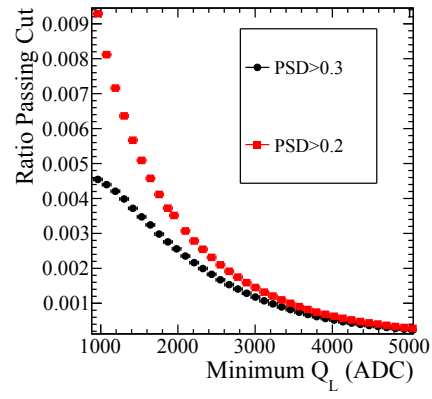
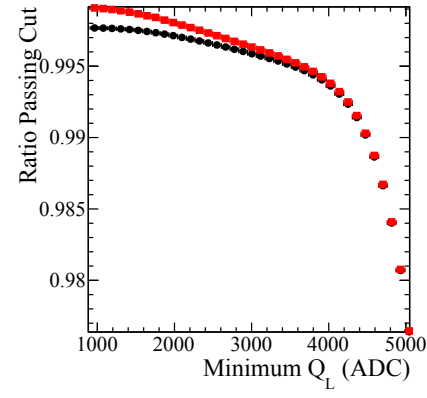


Figure 15: Neutron cut efficiency (top panel) and background contamination (bottom panel) for different cuts on Q_L . The red squares are with cut on $\text{PSD} > 0.2$, and the black circles are for a cut on $\text{PSD} > 0.3$

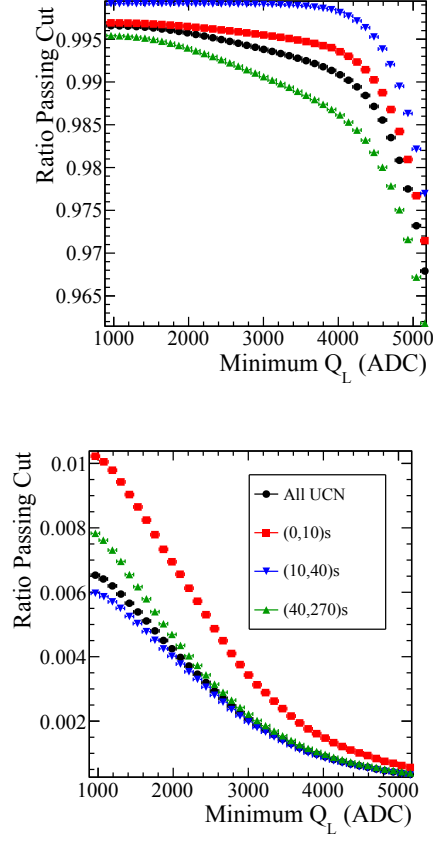


Figure 16: Neutron cut efficiency (top panel) and background contamination (bottom panel) for different times since the UCN production. The red boxes are for an average UCN rate of > 70 kHz over the first 10 s of UCN, the blue downward-triangles are for an average UCN rate of > 20 kHz over the next 30 s, and the green upward-triangles are for an average rate of < 10 kHz over the last 230 s.

the uncertainty in the absorption in the GS30 layer. The rate dependence of the efficiency is below the 0.5% level. This uncertainty could be improved by applying what we know about the statistics of random signals and backgrounds to model the expected rates. This would represent an improvement to the simple fit with unconstrained fractions of different types of pile-up described in this paper.

7. Conclusion

At high rates, the ^6Li detector had a higher counting efficiency than the Cascade detector. At later times in the UCN production cycle, which had a lower rate of UCN, the Cascade detector had a higher counting efficiency. This is explained as being due to the higher efficiency of the ^6Li detector for higher energy UCN reaching the detector soon after the UCN production. The lower efficiency at late times is due to a softer UCN spectrum at late times, and the higher Fermi potential of the lithium glass of 107 neV. The ^6Li detector has some sensitivity to background radiation, which is reduced by PSD cuts to a level of $0.3 \pm 0.1\%$ for the rates of background seen at PSI.

References

- [1] M. Pospelov and A. Ritz. Electric dipole moments as probes of new physics. *Annals of Physics*, 318, 2005.
- [2] *New searches for the neutron electric dipole moment*, PSI2013, 2013.
- [3] M. Wohlmuther et al. The spallation target of the ultra-cold neutron source ucn at psi. *Nucl. Instr. and Meth. A*, 564, 2006.
- [4] A.P.Serebrov et al. New measurements of neutron electric dipole moment with double chamber edm spectrometer. *JETP Letters*, 99, 2014.
- [5] A.P. Serebrov et al. *Physics Procedia*, 17, 2011.
- [6] K. Kirch. *AIP Conference Proceedings*, 1560, 2013.

- 354 [7] C.A. Baker et al. *Physics Procedia*, 17, 2011.
- 355 [8] Y. Masuda et al. *Physics Letters A*, 376, 2012.
- 356 [9] I. Altarev et al. *Nuovo Cimento C*, 35, 2012.
- 357 [10] R. Golub and S.K. Lamoreaux. *Physics Reports*, 237, 1994.
- 358 [11] Takeyasu M. Ito. Plans for a neutron edm experiment at sns. *J.Phys. Conf.*
359 *Ser.*, 69, 2007.
- 360 [12] M. Klein and C. J. Schmidt. Cascade, neutron detectors for highest count
361 rates in combination with asic/fpga based readout electronics. *Nucl. Instru.*
362 *and Methods in Particle Physics*, 628(1), 2011.
- 363 [13] G. Ban et al. *Nucl. Instr. and Meth. A*, 611(280), 2009.
- 364 [14] S. Afach et al. A device for the simultaneous spin analysis of ultracold
365 neutrons. *European Physical Journal A*, 51, 2015.
- 366 [15] B. Jamieson and L. A. Rebenitsch. Determining the 6li doped side of a
367 glass scintillator for ultra cold neutrons. *Nucl. Instru. and Methods A*, 790,
368 2015.
- 369 [16] B. Lauss. Ucn beamlines at psi. Psi internal document, Paul Scherrer
370 Institut, 2014.
- 371 [17] B. Lauss. Ultracold neutron production at the second spallation target of
372 the paul scherrer institut. *Physics Procedia*, 51, 2014.
- 373 [18] M. Senoville. Etude expérimentale d'un détecteur de neutrons capable
374 de mesurer de fort taux de comptage. Rapport de stage de m1 physique,
375 Université de Caen Basse-Normande, 2009.